Photocatalytic degradation of NO_x and ethanol in the gas phase by Spray Dried Ce-TiO_2

Hayat Khan[1,2], Mohamed Gar Alalm[2,3], Marc Lalonde-Lavoie[4], Marcela Frias Ordonez[4], Marta Sartirana[4], Alessia Giordana[5], Giuseppina Cerrato[5], Claudia L. Bianchi[5], Daria-Camilla Boffito[2,6*]

[1] Department of Chemical Engineering, University of Engineering & Technology, Peshawar, 25120, Pakistan

[2] Department of Chemical Engineering, Polytechnique Montréal, C.P. 6079, Succ. CV Montréal, H3C 3A7 Québec, Canada

[3] Department of Public Works Engineering, Faculty of Engineering, Mansoura University, Mansoura 35516, Egypt

[4] Università di Milano, Department of Chemistry, via Golgi 19, 20133 Milano, Italy

[5] Università di Torino, Department of Chemistry, via Pietro Giuria 7, 10125 Torino, Italy

[6] Canada Research Chair in Intensified Mechano-Chemical Processes for Sustainable Biomass Conversion

*daria-camilla.boffito@polymtl.ca

Abstract

We synthesized Ce doped TiO_2 (Ce_x-T) and tested it in the photocatalytic degradation of NO_x and ethanol under visible light. Pristine TiO_2 (T) and different dopant ratios of Ce-TiO_2 (Ce_x-T; x=0 to 1.0 wt%) were prepared by a water-based sol-gel method followed by spray drying. The successful doping of Ce in the lattice structure of TiO_2 was confirmed by several characterizations such as X-ray diffraction (XRD), energy dispersive X-ray (EDX), Fourier transform infrared (FTIR), and Raman spectroscopy. All the prepared catalysts grew as spherical grains with a polycrystalline anatase phase. $Ce_{0.8}$T revealed the lowest bandgap among all the prepared catalysts (2.8 eV) compared to 3.2 eV for T. The highest degradation of NO_x and ethanol was attained by $Ce_{0.8}$T (26±1 % and 23±1 %), which was 2.8 and 1.5 times the degradation by T, Furthermore, we proposed the photocatalytic degradation mechanism by the reactive oxidant species (ROS).

Keywords:

Cerium-doped catalyst; Ethanol; Nitrogen Oxides; Photocatalysis; Spray drying; TiO_2

Introduction

Photocatalysis recently emerged as a sustainable method for the degradation of recalcitrant compounds such as pharmaceuticals [1, 2], dyes [3, 4], perfluoroalkyl substances (PFAS) [5], and undesired gaseous emissions [6, 7]. The unselective nature of the reactive oxidant species (ROS) produced by photocatalysis leads to robust mineralization of refractory organics via different mechanisms [8, 9]. Currently, several families of photocatalysts compete for faster mineralization, higher stability, and harvesting a wider range of visible light [10]. These families include metal oxides [11], metal-organic frameworks (MOFs) [12], and carbonaceous-based catalysts [13]. Although the myriad of photocatalysts in the literature, the classical photocatalyst, TiO_2, still attracts many researchers due to its low cost and known safety [14]. However, TiO_2 is poorly active under visible light due to its relatively high bandgap (≈ 3.2 eV) [13]. Besides, the fast recombination of the photogenerated charges (i.e., electrons and holes) dissipates a considerable amount of energy [15].

The heterojunction photocatalysis was proposed to tackle the aforementioned limitations by the hybridization of two photocatalysts with different band structures [16]. By the contact interface of two semiconductors, the electron-hole route is changed into a different scheme (viz., Z-scheme or Schottky scheme), which reduces the effective bandgap and boosts the separation of charge carriers [15]. However, such heterojunctions are associated with the preparation of complex composites that require long synthesis procedures besides the cost and toxicity concerns [1]. Doping metals into the lattice of TiO_2 is another alternative to improve visible light absorption and reduce the recombination of charges [17, 18]. The doped metals add extra electronic levels in the wide bandgap of TiO_2 facilitating the transition of electrons from the valance band to the conduction band by a double excitation action [19].

Doping rare earth metals in the lattice of TiO_2 has not only shown a notable red shift of light absorption but also the hindrance of anatase transition into rutile during the calcination at high temperatures [20]. Among rare earth metals, cerium (Ce) is distinguished by the abundance in monazite and bastnaesite by 44% and 50% respectively [21, 22]. The electronic configuration of Ce^{3+}/Ce^{4+} ($4f^15d^0/4f^05d^0$) improves the electron acceptance by the reduction of electron-hole recombination, thereby enhancing the photostability and quantum yield [22]. Moreover, Ce doping generates labile oxygen vacancies (OVs) due to Ce^{3+}/C^{4+} charge balance in addition to the relatively high mobility of bulk oxygen species, which in turn leads to a strong catalytic potential [23]. Recent studies reported that the photocatalytic activity of Ce doped TiO_2 is dependent on Ce

concentration, distribution of Ce in crystals, adjustable crystallinity, developed functional groups, and the diffusion distance of e^-/h^+ pairs [24-26].

Several procedures were employed for the synthesis of Ce-TiO_2 including solvothermal [22], hydrothermal [26], flame spray pyrolysis [27], combustion [25], sol-gel [28], and single-pot microemulsion [29]. The sol-gel method is distinguished by straightforward procedures with less cost and working under relatively low temperatures [30]. Several studies reported the synthesis of Ce-TiO_2 nanoparticles using ethanol as a solvent in the sol-gel process [23, 24, 30], whereas the water-based sol-gel synthesis is scarcely reported.

In the present study, we report for the first time the synthesis of porous Ce doped TiO_2 (0-1.0 wt. %) microspheres with narrowed bandgaps via water-based sol-gel technique followed by spray drying. With this novel procedure, we obtained clear regular and uniform sphere-like particles. Furthermore, the characterization of structural, textural, morphological, optical, and electronic properties confirmed the successful growth of this novel catalyst. The degradation of ethanol (a volatile organic compound, VOC) and NO_x conversion in the gas phase were studied for the first time to evaluate the performance of the prepared photocatalysts. We also proposed the degradation mechanism and explained the role of narrowed bandgap and reduced recombination rate in the photocatalytic process. The results are promising for future applications of Ce-TiO_2 as air pollution control, indoor surface coverings, gas sensors, and solar cells.

2. Materials and Methods

2.1. Chemicals

Titanium butoxide ($Ti(C_4H_9O)_4$ purum ≥ 97.0% gravimetric), cerium nitrate hexahydrate ($Ce(NO_3)_3.6H_2O$, 99.999 %), formic acid (reagent grade ≥ 95 %) were purchased from Sigma Aldrich, Canada. All chemicals were used as received without further treatment.

2.2. Catalyst preparation

Pristine TiO_2 was synthesized by the sol-gel method reported elsewhere [28]. Briefly, titanium butoxide (10 ml), water (30 ml), and formic acid (1 ml) were mixed for 120 min using a magnetic stirrer at ambient temperature. The deionized water was added dropwise to titanium butoxide forming a milky sol of titanium hydroxide by the polymerization and hydrolysis/condensation reactions, then formic acid was added drop-wisely. The sol solution was aged for gelation for 5 h at ambient temperature followed by spray drying using a Yamato GB-22 dryer producing hot air

at 130 ^{o}C in a glass chamber (Diameter: 132 mm x height: 577 mm) to obtain the final TiO_2 powders. The slurry was automized with two stainless steel fluid nozzles (1.270 mm for the gas and 0.406 mm for the slurry), the slurry was fed to the chamber by a peristaltic pump at 3.0 mL min^{-1} under a gas flow rate of 0.3 m^3 min^{-1}. Finally, the collected dried powder was calcined at 500 °C in a muffle furnace for 2 h with a rate of 3 ^{o}C/min to obtain the crystalline TiO_2 [31-33].

We synthesized the Ce doped TiO_2 powders using a similar procedure as for pristine TiO_2, but by introducing the Ce precursor in water before adding it to the titanium butoxide. The weight ratios of Ce to TiO_2 were set as 0%, 0.2%, 0.4%, 0.6%, 0.8%, and 1.0% and the final products were denoted as T and Ce_x-T, where x is the Ce weight ratio.

2.3. Characterization

X-ray diffraction (XRD) was analyzed by (Phillips PW 1710, using high-intensity Cu Kα monochromatic radiation (λ = 0.15418nm)) to study the crystalline phases and determine the crystallite size. A Bruker Tensor 27 with OPUS data collection program (V 1.1) and DTGS detector was used to record the Fourier transform infrared (FTIR) spectra in the 5000-400 cm^{-1} frequency range and with 1 cm^{-1} resolution. The calcined powder was mixed with potassium bromide (KBr) reference. A scanning electron microscope (SEM-JEOL JSM-7600F) acquired the microscopy images and energy dispersive X-ray (EDX) in order to investigate the morphology and elemental composition. Transmission electron microscopy (TEM) was conducted using a Phillips Technai G2 20TEM operated at 200 kV. The textural properties of the prepared powders were analysed on a Quantachrome Autosorb-1 Instrument by measuring the N2 adsorption and desorption isotherms at 77 K, after degassing the sample under vacuum at 200 °C for 20 h. Photocatalyst specific surface area and pore diameter were determined by nitrogen adsorption desorption isotherm using BET (Brunauer–Emmett–Teller) method (P/P_0: 0.05–0.30, C constant: 50–200) and the Barrett-Joyner-Hallender (BJH) theory was used to measure the pore diameter (desorption branch, P/P_0: 0.15–0.995). Raman spectra at room temperature were detected by a Renishaw RM3000 Micro-Raman system with an excitation laser wavelength of 514 nm, 300 mW laser power and 10 s as exposure time and the resolution was 1 cm^{-1} The sample powder film on glass substrate was firmly pressed to have a uniform and smooth surface, during analysis different areas (2-3 per sample) were analyzed to be certain for the obtained Raman spectra. Elemental composition and valance states analysis were conducted by X-ray photoelectron spectroscopy (XPS) (Thermo Scientific K-alpha, USA) employing Al Kα (1486.6 eV) X-rays. First, a survey

spectrum was recorded to identify the elements present in the sample, followed by a high-resolution spectrum of the identified elements at pass energy of 20 eV and 0.05 eV steps. The Advantage (Thermo Scientific) software processed the spectrum data. Diffuse reflectance spectra (DRS) were obtained by a UV/Vis (Evolution 300) with attaching a Praying Mantis^{TM} diffuse reflection (DRIFTS) accessory in the range of 190-600 nm, taking potassium bromide (KBr) as a reference, then Tauc plots were used to determine the bandgap of the samples.

2.4. Photocatalytic experiments

The photocatalytic films were deposited by drop-casting 0.050 g of catalyst dispersed in i-propanol on glass plates (200 mm x 20 mm for NO_x and 100 x 100 mm for ethanol). In both cases, the coated plates were placed at the bottom of the reactors.

The photocatalytic degradation of NO_x took place inside a 20 L Pyrex glass cylindrical reactor in the static gas phase under visible light irradiation [34]. The gas mixture was prepared by mixing NO_2 with (40%-50%) humidified air. The initial inlet gas is pure NO_2, which was partially decomposed into NO until the chemical equilibrium is established. Consequently, the photocatalytic reactor contained a mixture of NO and NO_2 with an initial concentration of 500 ± 50 ppb. The reactor was irradiated by a LED lamp (350 mA, 9-48 V DC, 16.8 W) with an emission range of 400-700 nmbn yielding an intensity of 1000 lx on the catalyst surface. The NO and NO_2 concentrations were instantaneously monitored during the reaction by an Ecotech Serinus 40NO_x. The experiments were conducted at 25 °C for a reaction time of 180 min. The photolysis experiments revealed negligible degradation (< 5% in 180 min).

The degradation of ethanol was conducted in a 5 L Pyrex glass reactor with four openings connected to a gas chromatograph (Agilent 3000 A Micro-GC, Santa Clara, CA, USA) for simultaneous monitoring of organic content, CO_2, and other by-products as reported elsewhere [35]. The gaseous mixture in the reactor was obtained by mixing chromatographic air, humidified at 40% at room temperature, and a fixed amount of volatilized ethanol to obtain an initial concentration of 400 ppm. The reactor was equipped with a hygrometer to monitor the relative humidity. A similar LED lamp irradiated the coated catalyst plates by an intensity of 5200 lx. The ethanol was monitored during dark and photolysis tests to confirm the photocatalytic degradation mechanism. The inert gas was used to clean up the reactor and dispose of CO_2 traces.

3. Results and Discussions

3.1 Material characterization

The XRD patterns of control, representative $Ce_{0.8}$-T are shown in Fig. 1a, while rest of the doped samples (Ce_x-T, x = 0.2, 0.4, 0.6 and 1.0 wt. %) XRD are displayed in Fig. S1 (supplementary information). The diffractograms showed diffraction peaks at 2Θ of 25.4°, 37.1°, 37.9°, 38.6°, 48.2°, 54.0°, 55.2°, 62.2°, and 68.9°, which were indexed to (101), (103), (004), (112), (200), (105), (211), (204) and (116) crystal planes of the pure anatase phase of tetragonal TiO_2 (JCPDS No: 21-1272) in all samples, respectively. The absence of Ce peaks in the XRD patterns was ascribed to the low percentage in the samples. Furthermore, no peaks for cerium oxides (CeO_2) were detected suggesting the effective doping of Ce into the lattice structure of TiO_2. The ionic radii of Ce^{3+} and Ce^{4+} (0.103 and 0.093 nm, respectively) are larger than that of Ti^{4+} (0.068 nm), so the substitution of Ti by Ce in the TiO_2 crystal lattice is limited. Therefore, a low number of Ce^{3+}/Ce^{4+} species may penetrate the lattice, whereas the remaining dopant ions were distributed in the grain boundary/grain junctions [36]. XRD spectra indicated that no rutile or brookite phase appeared after doping, suggesting the stability of TiO_2 crystal structure with doping. The average crystallite size of all samples (Table 1) was determined by the Scherrer's formula ($D = \frac{0.9\,\lambda}{\beta\, Cos\theta}$, where λ is the X-ray wavelength, θ is the Bragg angle, and β is the full width at half maximum (FWHM)) taking the diffraction plane (101) of pure and Ce doped powders. No considerable difference was observed for the samples of Ce percentage ≤ 0.8% and all samples had an average crystallite size close to 40 nm. The reasons for the control size may be ascribed to: (i) the segregation of the Ce cations to the grain boundary, which hinders the growth of the nano crystallite in the nanoparticles due to the formation of Ce-O-Ti bonds or (ii) probably due to the Ce species adsorption on the surface of primary TiO_2 particles, or (iii) the Ce ions can absorb more energy from its different energy levels to reduce the surface energy of titania particles, which slowdowns the aggregation process of the particles [22, 28]. The crystallite size of $Ce_{1.0}$T increased to 41.0 nm, which may be imputed to the higher dopant content that reduces the uniformity of nanoparticles, and consequently increases the atomic attractive forces leading to the agglomeration of crystals in larger grains [37].

The control size of the Ce_x-T (x = 0.2 – 0.8 wt. %) powders with respect to pure T was confirmed by the Raman analysis (Fig. 1b) with the constant full-width at half-maximum (FWHM) value of 9.57±0.07 at the 1-Eg (142.6 nm) peak. Moreover, in line with the XRD analysis, Raman results depict the pure anatase phase showing distinct representative peaks at 142.6 cm^{-1} (1-Eg),

196.2 cm^{-1} (2-Eg), 393.3 cm^{-1} (B1g), 514.3 cm^{-1} (A1g), and 637.5 cm^{-1} (3-Eg). Besides, the sharpness and high intensity of these peaks suggest high crystallinity, which is beneficial for photocatalytic activity by minimizing crystalline defects. Yang et al. [38] reported that (001) planes in anatase TiO_2 are very active due to their complete unsaturated Ti atoms and high surface energy (0.9 $J.m^{-2}$), which further increase the adsorbability, stability, and catalytic activity. Raman spectroscopy determined the percentage of the exposed (001) anatase planes. The Raman peak intensity ratios of 1-E_g (144 cm^{-1}) and A_{1g} (517.4 cm^{-1}) modes were taken into account (Fig. 1b) [39]. An increase to 11.7 % was observed for the $Ce_{0.8}T$ sample, but it was reduced with the further increase of the Ce percentage (Table 1).

Table 1. Crystallite size, BET surface area, cerium surface density, percentage of [001] planes, and bandgap energy of the differently prepared photocatalysts.

Sample	Crystallite size* (nm)	BET surface area* (m^2/g)	Pore dia (nm)	Ce_{sd} (atom nm^{-2})	Percentage of [001] planes†	Band gap* (eV)
T	12.8	12.2	1.8		6.0	3.2
$Ce_{0.2}$-T	12.7	13.7	1.7	1.5	6.3	3.18
$Ce_{0.4}$-T	12.7	13.5	2.2	2.7	6.5	3.1
$Ce_{0.6}$-T	12.6	15.2	2.6	4.1	7.6	3.0
$Ce_{0.8}$-T	12.8	16.1	2.9	5.1	7.9	2.8
$Ce_{1.0}$-T	12.5	14.5	2.3	7.0	6.8	3.0

* The uncertainty in the; crystallite size is < 0.2 nm, surface area is < 0.5 m^2/g, bandgap is < 0.3 eV

† Ratio of Raman vibrational modes 1-E_g (144 cm^{-1}) / A_{1g} (515 cm^{-1})

In a quest for investigating the surface terminations (i.e., functionalities) of the systems of interest, the catalyst has been analyzed by FTIR spectroscopy (Fig. 1c). At least four spectral regions suggest peculiar and ubiquitous surface species: (i) a large unresolved envelope located at $\nu > 3000$ cm^{-1} due to the OH species that mutually interacted with H-bonding, for instance, those relative to undissociated molecular water whose spectroscopic counterpart is located at 1630 cm^{-1}. (ii) a sharp component is present at $\nu \sim 3700$ cm^{-1} due to the stretching mode of all Ti–OH species free from hydrogen bonding interactions [40-42]. (iii) In the 3000-2800 cm^{-1} spectral range some minor components are evident and can be ascribed to the C-H stretching vibration of ubiquitous hydrocarbons. (iv) In the 1500-1300 cm^{-1} spectral range some components are also present which might be ascribed to either carbonate or carboxylate surface species. These species may be resulted as a residue of the preparation route or due to the exposure of the powders to

atmospheric CO_2 after the calcination step.

The optical absorption properties were examined by UV–vis DRS and the bandgaps were determined (Table 1) by Tauc plots (hυ versus αhν)$^{1/2}$) shown in Fig. 1d. The bandgap of TiO_2 was reduced from 3.2 to 2.8 eV as the Ce was introduced by 0.8% wt. suggesting a broader absorption range. This red shift promotes the photocatalytic activity under visible light. Cerium can store/release oxygen through the redox shift between Ce^{3+}/Ce^{4+} under reduction and oxidizing conditions, respectively [43]. The Ce 4f level is positioned about 2–3 eV above the valence band near the oxygen defect level (2.88 eV) [44]. Hence, Ce inclusion into the TiO_2 lattice structure generates 4f (Ce^{3+}/Ce^{4+}) impurity bands and oxygen defect states, as vacancies, which hybridize to form an impurity level below the conduction band. This may result in a redshift of the doped nanomaterials towards longer wavelengths, and a narrower bandgap.

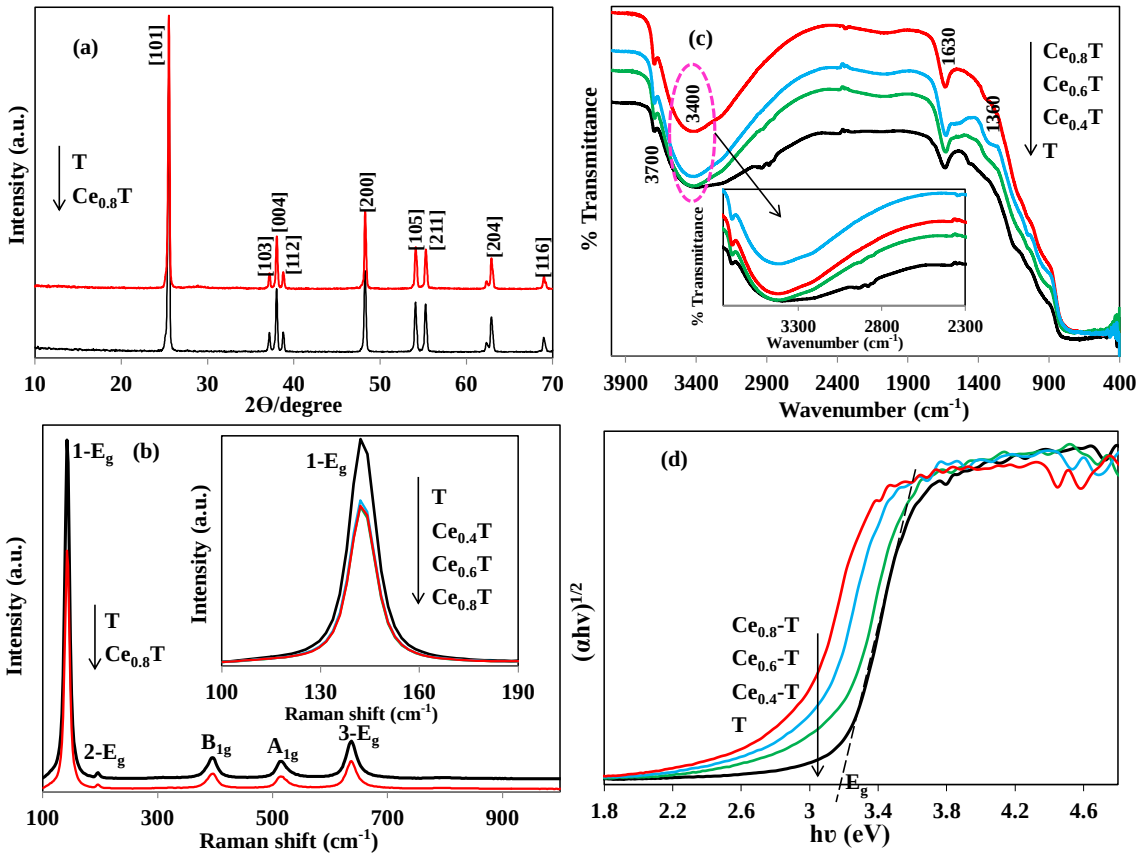

Fig.1. (a) X-ray diffractograms of the representative pure (T) and Ce-doped ($Ce_{0.8}$-T) TiO_2, (b) Raman spectra of T and $Ce_{0.8}$T (insert - Raman 1-E_g mode) powders, (c) FTIR spectra of pure (T) and Ce_x doped (x = 0.4, 0.6 and 0.8 wt. %) TiO_2 (insert – the magnified image of the pointed areas

in the main spectra) and (d) Tauc plots of the representative (T, $Ce_{0.4}$-T, $Ce_{0.6}$-T and$Ce_{0.8}$-T) samples. All the powders are calcined at 500^{o}C.

The high-resolution SEM micrographs of the $Ce_{0.8}$-T and pure T are shown in Fig. 2 (a, b) and Fig. S2 (supplementary information). They reveal that all the photocatalyst particles (pure and Ce doped) are homogenous, agglomerated, and of spherical shape. The mean size of the spheroids observed with SEM was 152.8 nm for $Ce_{0.8}$T and 153.0 nm for T, which is bigger than the crystallite size (34 nm for both Ce_x-T and T) indicating that each particle was assembled from many crystals. SEM images further indicate that TiO_2 primary crystallites tend to agglomerate in a ball-like shape with the stated experimental method dissimilar to the conventional sol-gel procedure that usually develops irregular shape. The SEM results are further supported by the HR-TEM analysis (Fig. 2c,d) as the particle size did not change with Ce doping. This allows us to preliminary classify this Ce-TiO_2 system as micrometric. It is important to evidence that upon Ce doping; the anatase phase is confirmed to be the only TiO_2 polymorph observed (main family planes due to (101) [ICDD card n. 21-1272], as stated by the selected area electron diffraction patterns (SAED), which also further specifies the crystalline nature of the photocatalyst microsphere in line with XRD observations. The elemental mapping by EDX (Fig. S3, supplementary information) reveals that Ce is evenly distributed through the photocatalyst sample; the Ce doping is also evident from Fig. 2d (insert). The excellent homogeneity of Ce in TiO_2 is because of; the spray-dryer nozzle atomized fine uniform size droplets of the sample precursor dry instantaneously by stream of hot air (110 ^{o}C).

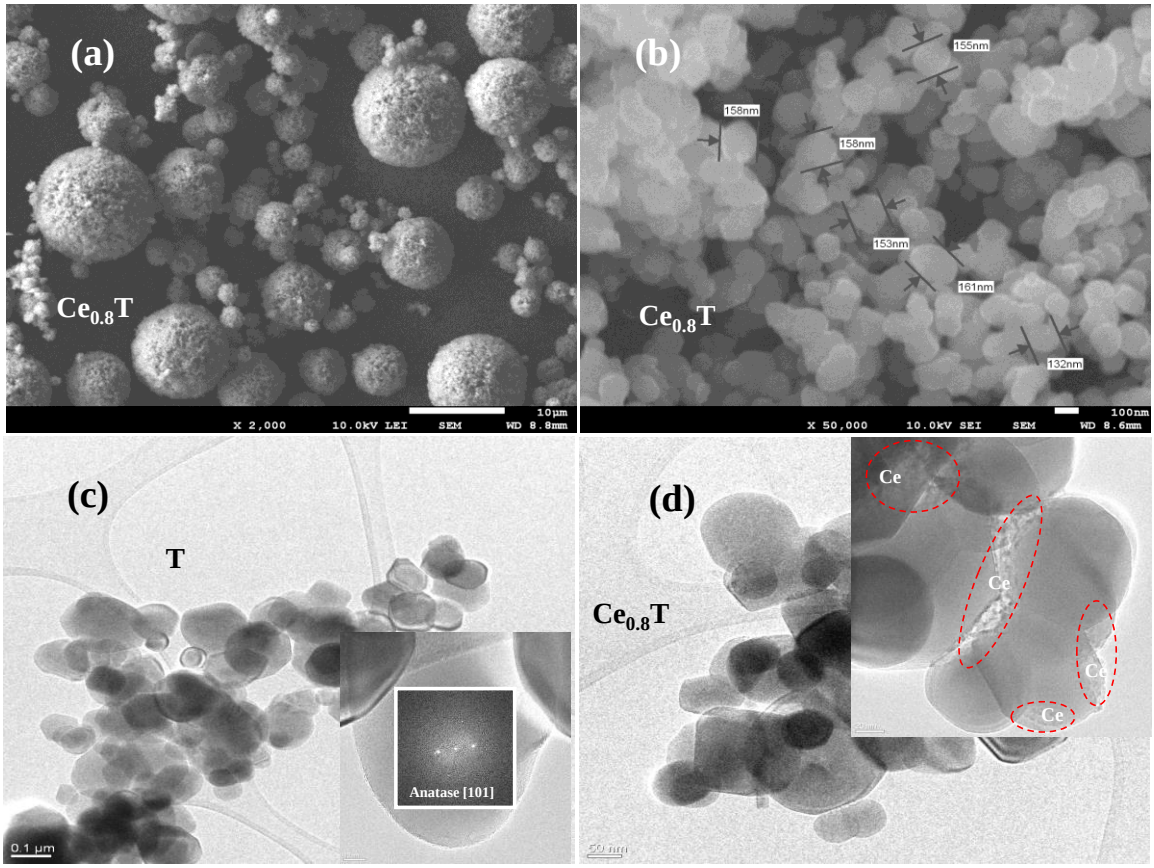

Fig.2. (a, b) SEM micrographs of the calcined $C_{0.8}$-T sample, TEM images of calcined (c) pure (T) (insert – SAED pattern), and (d) $Ce_{0.8}$-T (insert – dotted region shows the presence of Ce doping) powders.

The values of S_{BET} for control T and Ce_x-T are illustrated in Table 1. Ce_x-T surface area slightly increased than that of T up to a Ce percentage of 0.8% wt., but the further increase of the Ce percentage resulted in a reduction in the surface area. The $Ce_{0.8}$-T sample has the largest S_{BET} (16.1 m^2/g) compared to control T (12.2 m^2/g) and other Ce_x-T samples. The BjH pore diameter (Table 1) slightly increased at higher Ce content up to 0.8 % but decreased at 1.0%. The increase of the pore size of Ce_x-T powders is expected to improve the diffusion of pollutant molecules, thereby enhancing the sorption of parent and intermediate products during the photocatalytic reaction [16]. The Ce surface density of each sample was determined by the equation ($Ce_{sd} = \frac{\%\, mass\ of\ Ce * NA}{S_{BET} * MM_{Ce}}$) [26] illustrating quantity of Ce atoms per unit area distributed over the materials surface, where Ce_{sd} is the number of Ce atoms per square nm of material surface area, % mass of Ce is the nominal mass percentage of Ce doping, NA is Avogadro's number ($6.022*10^{23}$), S_{BET} is the surface area (nm^2/g), and MM_{Ce} is the molar mass of the Ce (mol/g). As expected, the results

shown in Table 1 indicate that Ce surface density is dependent on S_{BET} and Ce percentage.

To understand the composition and chemical nature of Ce doping in TiO_2 microspheres, the electron bonding energies of O 1s, Ti 2p, Ce 3d were investigated in reference to C 1s peak by XPS (Fig. 3). The spectrum of $Ce_{0.8}T$ (Fig. 3a) reveals the presence of all the stated elements. The atomic percentages of these elements were 52.0%, 32.0%, 3.0%, and 13.0% for O, Ti, Ce, and C, respectively. We further analyzed the XPS spectrum of the $Ce_{0.8}T$ by high-resolution deconvolution of the C (1s), O (1s), Ti (2p), and Ce (3d). In the core level XPS spectrum of C 1s, the dominant peak was observed at 284.2 eV (C-C), which is imputed to the adventitious carbon from the XPS instrument. The other peaks at 286.0 and 285.5 eV represents C-O-C and Ti-O-C groups. The peak at 282.5 eV may be ascribed to the chemical bonding between carbon and titanium [45] or the carbide formation during analysis [46]. In the high-resolution spectrum of O 1s, the main peak at 530.2 eV is a typical of metallic oxides, which arises from the overlapping contributions of oxygen from TiO_2 and Ti-O-Ce, but the oxygen from TiO_2 is the primary contributor. The peaks at 531.0 and 532.0 eV are attributed to the hydroxyl groups on the material surface. The peaks at 528.6 and 527.3 eV are imputed to Ti-O and oxygen vacancy (V_o) [47]. From the Ti 2p XPS spectrum, the spin-orbit components ($2p_{3/2}$ and $2p_{1/2}$) of the peak were well deconvoluted by three peaks. The 465.3 and 459.5 eV binding energy signifying that the Ti element mainly existed in the chemical state of Ti^{4+}. The peaks at 463.3, 457.5, 455.6, and 460.1 eV are ascribed to the reduced Ti^{3+} and Ti^{2+} states in the TiO_2 lattice [16, 48]. The reduced states may appear from a charge imbalance caused by the Ce ions being localized in the octahedral interstitial site during the annealing process. The photoelectron spectrum of Ce 3d is rather complex owing to the hybridization of Ce 4f and O 2p electrons. The Ce 3d core level can be attributed to the spin-orbit split doublets states of $3d_{3/2}$ and $3d_{5/2}$. The peaks at 888.4 and 907.0 eV refer to Ce^{3+}, The signals at 882.9 and 900.4 eV are due to the presence of Ce^{4+}, whereas the peaks at 885.8 and 903.6 eV indicate the existence of Ce [49]. The peaks at 879.4 and 899.2 eV resulted from the transfer of one or two electrons from O 2p filled orbit to Ce 4f empty orbital [50]. In summary, the XPS investigation clearly demonstrates the presence of dopant impurity level Ce^{3+}/Ce^{4+}, reduced states of Ti (Ti^{3+}/Ti^{2+}), and oxygen vacancy states.

All the aforementioned characterization results indicate the successful synthesis of Ce_x-T catalysts using the water-sol-gel method and spray drying. As an ethanol-free method, the water-sol-gel is favored as an eco-friendly procedure for TiO_2 synthesis at ambient temperature without

any deficiency in photocatalytic activity. Furthermore, the treatment by spray drying offers the uniform growth of the catalyst nanoparticles compared to conventional oven drying.

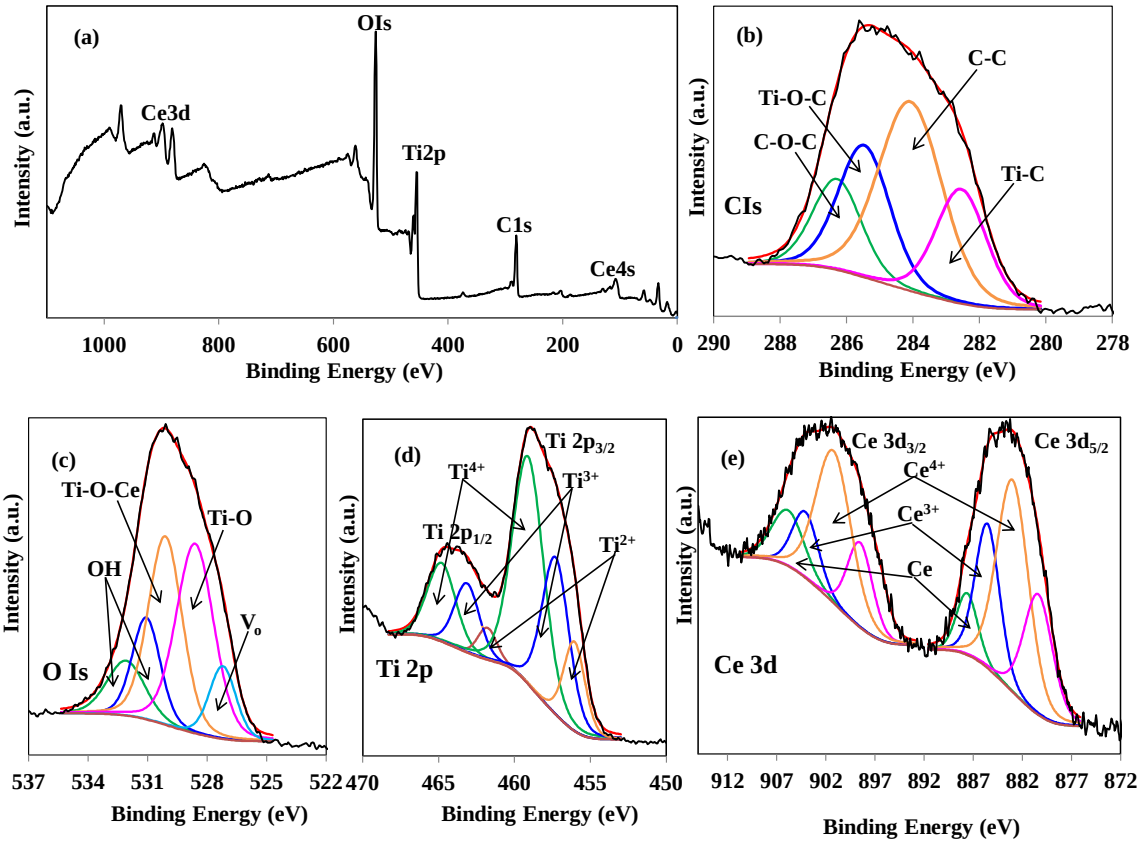

Fig. 3. (a) XPS survey spectrum and high resolution spectra of (b) C1s, (c) O1s, (d) Ti2p, (e) Ce3d of the representative calcined $Ce_{0.8}$-T powder.

3.2 Photocatalytic Activity

The photocatalytic activity of the different control and doped samples was evaluated by the degradation of NO_x and ethanol (Fig. 4) as model pollutants in the gas phase. All Ce_x-T samples showed an enhanced photocatalytic NO_x reduction compared to bare TiO_2. The highest NO_x degradation was obtained by $Ce_{0.8}$T and $Ce_{1.0}$T (26±1 %), which is 2.8 times greater than the photocatalytic efficiency of T in 180 min of irradiation. Other Ce doped catalysts (Ce_x-T) also showed remarkably improved photocatalytic activity. It is also noted that this improvement was relative to the Ce content, which confirms the Ce role in the photocatalytic reaction. The enhanced photocatalytic activity is attributed to narrowed energy bandgap due to the insertion of Ce ions in the structure of TiO_2 as confirmed by UV-DRS analysis and XPS. Furthermore, Ce ions act as an

electron trap wherein the photogenerated electrons on the conduction band of TiO_2 can be transferred to Ce ion, which reduces the recombination of electron/holes charges [22]. Moreover, FTIR spectroscopy detected surface hydroxyl groups which convert the photogenerated holes to hydroxyl radicals ($OH^{\bullet}$) improving the photocatalytic activity. The greater anatase [001] planes improve the adsorption of the pollutant to the active catalyst surface [51]. Figure 4b depicts the ethanol degradation under the LED light. After 180 min of irradiation, the photocatalytic degradation by control T was 15±1 %, whereas all the Ce_x-T samples exhibited greater performance. The highest activity was achieved by $Ce_{0.8}T$ (23±1 %) whereas a slight decrease in the photocatalytic activity was found by $Ce_{1.0}T$. Like the behavior of NO_x, other Ce doped catalysts (Ce_x-T) also showed an enhanced photocatalytic activity relative to the amount of doped Ce. Similar observations were reported by Fan et al. [52] wherein Ce ions at higher load can play as recombination center instead of electron trap.

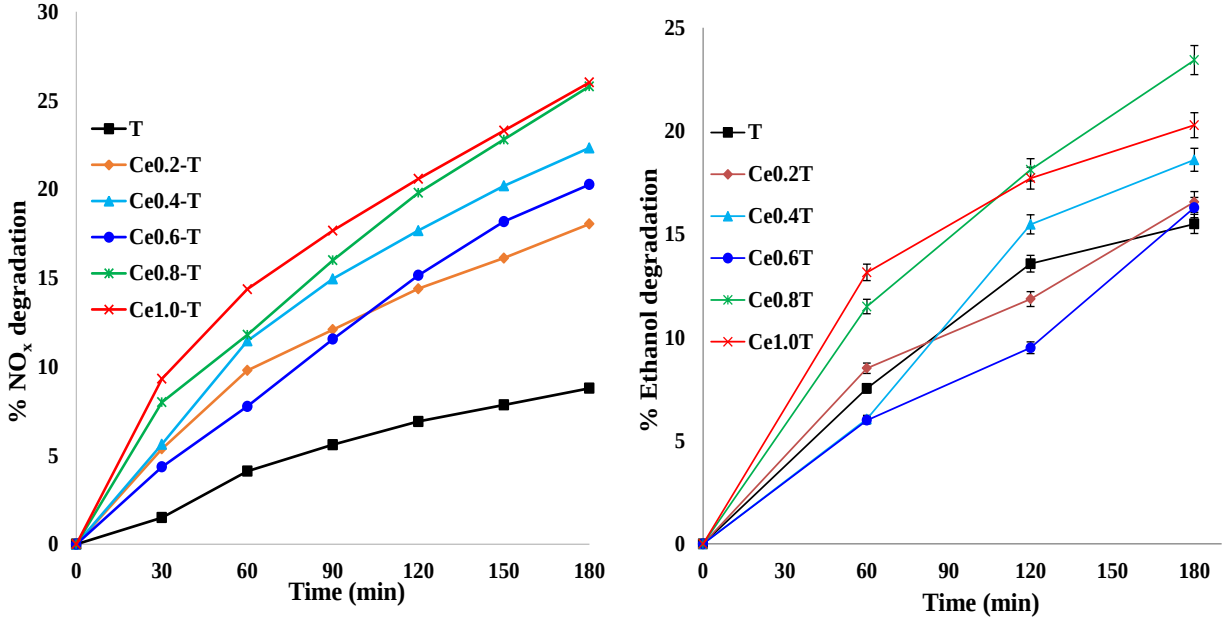

Fig. 4. Visible photocatalytic activity of the prepared samples against the model pollutants (a) NO_x and (b) ethanol decomposition in the gas phase.

3.3 Proposed Mechanism

We propose the following photogenerated charge carrier scheme based on the performed characterization study. Visible photoinduced electron-hole (e^-/h^+) pairs produced in the conduction band (CB) and valance band (VB) are represented by black dotted lines in Fig. 5. The synthesized $Ce_{0.8}$-T, and $Ce_{1.0}$-T, catalysts showed the highest activity for the gas phase

decomposition of the model pollutants NO_x and ethanol under visible light in that order. The VB holes react with the chemisorbed water and OH groups on the catalyst surface to generate the hydroxyl radicals ($OH^{\bullet}$), whereas the CB electrons react with oxygen to produce superoxide anion radicals ($O_2^{\bullet-}$) which through a series of reactions leads to the formation of OH^-, H_2O_2, $HO^{\bullet}$ species, participating in the decomposition of the pollutant molecules.

UV-vis DRS and XPS spectroscopy revealed that Ce inclusion into TiO_2 results in the formation of Ce^{4+}/Ce^{3+} impurity levels which not only reduce the bandgap but also act as a trap of electrons ($Ce^{4+} + e_{CB}^- \rightarrow Ce^{3+}$; $Ce^{3+} + O_{2\,abs} \rightarrow O_2^{\bullet-} + Ce^{4+}$) to retard the recombination of charges. XPS analysis shows the presence of defect states; Ti^{3+}, Ti^{2+} (Ti reduced states), and oxygen vacancies (V_o) which also promote the charge transfer and photons absorptions in the visible region. The Ti^{3+} defect level on the surface or in the bulk can suppress the photogenerated electron-hole pairs recombination and extend their lifetime ($Ti^{4+} - OH + e_{CB}^- \rightarrow Ti^{3+} - OH^-$; $Ti^{3+} - OH + h^+ \rightarrow Ti^{4+} - OH^{\bullet}$) [21]. The trapped electron of Ti^{3+} may also transfer to the Ce^{4+} resulting in the formation of Ce^{3+} because the electrode potential of Ti^{4+}/Ti^{3+} (-0.02 V) is more negative than that of Ce^{4+}/Ce^{3+} (1.4 V) [53]. In oxygen-rich environments with bulk Ti^{3+} defects, the excess charge can easily be withdrawn by the surface adsorbed oxygen, which could be diffused from the surface to the bulk via gradually filling the bulk oxygen vacancies [54]. The trapped conduction electrons in the oxygen vacancies (V_o) interact with the OH^- acceptor level to produces $OH^{\bullet}$ radicals [55]. Moreover, it is reported that the Ti reduced species play an important role in visible light absorption and the adsorption of both molecular and dissociative channels existing at defect levels with the charge transfer from reduced Ti [56, 57].

In summary, the existence of Ce^{4+}/Ce^{3+} impurity level, Ti reduced states (Ti^{3+}/Ti^{2+}), oxygen vacancies (V_o), and reduced the TiO_2 band gap induced a red-shift that enhanced the photocatalytic activity under visible light. They also improved the trapping of the photogenerated electrons via inhibiting the recombination of charges as a consequence results in the formation of $OH^{\bullet}$ radicals. It is worth noting that the abundance of surface hydroxyl groups (OH^-) on the surface of TiO_2 microspheres was beneficial to photocatalytic activity.

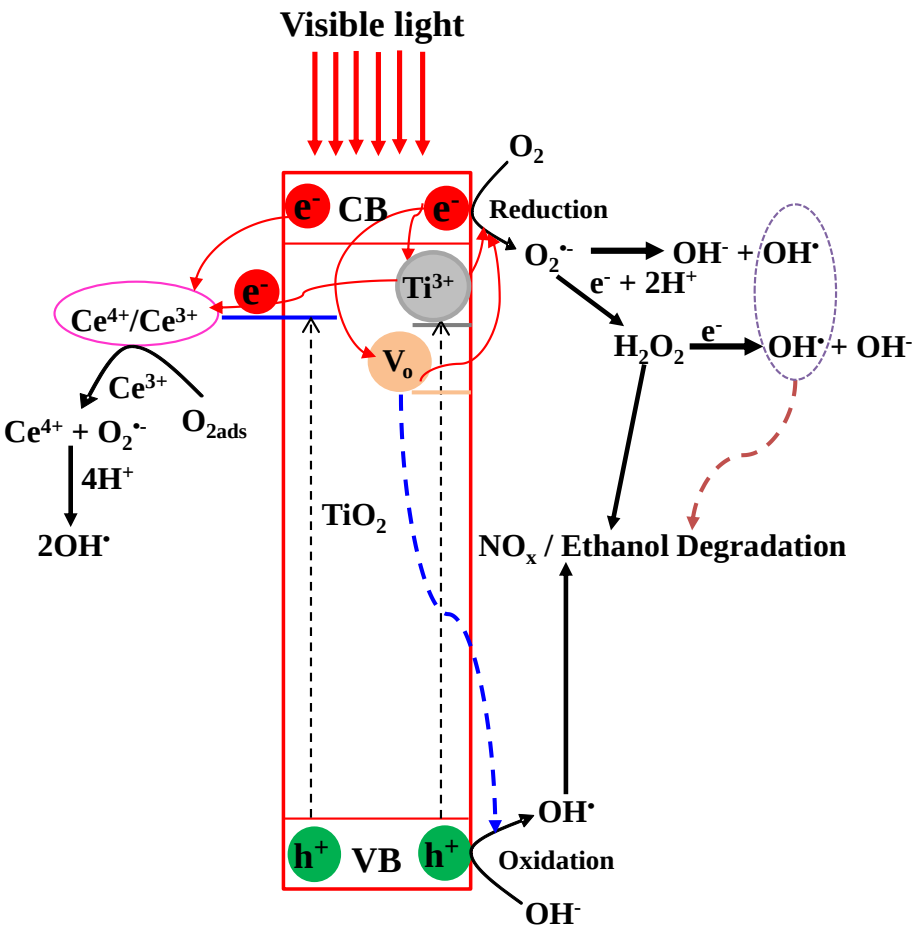

Fig. 5. Proposed mechanism illustrating the transfer pathways of the visible light-induced electron-hole pairs contributing towards model pollutant (NO_x/ethanol) molecules decomposition.

4. Conclusion

In this study, control and Ce-doped TiO_2 microsphere were successfully prepared by the sol-gel method with ratios of Ce to TiO_2 0%, 0.2%, 0.4%, 0.6%, 0.8%, and 1.0%. We introduced a novel eco-friendly procedure comprises an ethanol-free sol-gel method and spray drying instead of conventional oven drying. The resulting material possesses a stable crystallite anatase phase of uniform size with the inclusion of cerium dopant. The Ce-doped TiO_2 catalysts were more active under visible light than pristine TiO_2. Further, it was revealed that dopant impurity level (Ce^{3+}/Ce^{4+}), Ti reduced states (Ti^{3+}/Ti^{2+}), and oxygen vacancies (V_o) reduced the recombination of photoinduced electron-hole pairs. In summary, the defined synthesis method brings the unique interaction among anatase TiO_2 reduced states, Ce impurity levels, and V_o species. Accordingly,

the NO_x degradation by $Ce_{0.8}T$ was 2.8 times greater than pristine T. Other Ce doped catalysts (Ce_x-T) improved the photocatalytic activity relative to Ce content, and similar trends were observed during ethanol degradation. We suggest employing this water sol-gel method with spray drying for doping other metals in TiO_2 structure in future studies to reduce the usage of chemicals and obtain more uniform nanoparticles. In addition, spray drying operation is simple, cost effective and has the potential to be used for the continuous synthesis of uniform structured photocatalyst at large scale. In summary, current study can provide theoretical and practical insight into the enhancement of TiO_2 photocatalytic activity against volatile, toxic and hazardous gaseous pollutants by a lanthanide series metal doping method.

Conflicts of Interest

All the authors certify that there is no conflict of interest to declare regarding the publication of this paper.

Acknowledgments

The authors are greatly thankful to the Natural Sciences and Engineering Research Council of Canada (NSERC) and the Fonds de recherche du Quebec – Nature et technologies (FRQNT) to provide support for this research, as well as to the Canada Foundation for Innovation (CFI) This research was undertaken, in part, thanks to funding from the Canada Research Chairs program. M.G.A is supported by Velux Stiftung Foundation through the project 1381 SUNFLOAT–Water decontamination by sunlight-driven floating photocatalytic systems.

References

[1] K. Fouad, M.G. Alalm, M. Bassyouni, M.Y. Saleh, A novel photocatalytic reactor for the extended reuse of W–TiO_2 in the degradation of sulfamethazine. Chemosphere, 257 (2020) 127270.
[2] S. Ahmadi, Z.S. Mahmoudabadi, A. Khoshroo, K. Tabar-Heydar, Electrochemical and catalytic investigations of epinephrine, acetaminophen and folic acid at the surface of titanium dioxide nanoparticle-modified carbon paste electrode. Ionics 20 (2014) 1757-1765.
3] Y. Liu, Y. Ohko, R. Zhang, Y. Yang, Z. Zhang, Degradation of malachite green on Pd/WO_3 photocatalysts under simulated solar light. J. Hazard. Mater. 184 (2010) 386-391.
[4] M.F. Sanad, A.E. Shalan, S.M. Bazid, S.M. Abdelbasir, Pollutant degradation of different organic dyes using the photocatalytic activity of ZnO@ZnS nanocomposite materials. J.

Environm. Chem. Eng. 6 (2018) 3981-3990.
[5] B. Gomez-Ruiz, P. Ribao, N. Diban, M.J. Rivero, I. Ortiz, A. Urtiaga, Photocatalytic degradation and mineralization of perfluorooctanoic acid (PFOA) using a composite TiO_2–rGO catalyst. J.Hazard. Mater. 344 (2018) 950-957.
[6] C. Pirola, D.C. Boffito, S. Vitali, C.L. Bianchi, Photocatalytic coatings for building industry: study of 1 year of activity in the NO_x degradation. J. Coatings Technol. Res. 9 (2012) 453-458.
[7] M. Stucchi, C.L. Bianchi, C. Argirusis, V. Pifferi, B. Neppolian, G. Cerrato, D.C. Boffito, Ultrasound assisted synthesis of Ag-decorated TiO_2 active in visible light. Ultrason. Sonochem. 40 (2018) 282-288.
[8] J.H. Martínez-Montelongo, I.E. Medina-Ramírez, Y. Romo-Lozano, J.A. Zapien, Development of a sustainable photocatalytic process for air purification. Chemosphere 257 (2020) 127236.
[9] K. Sornalingam, A. McDonagh, J.L. Zhou, M.A.H. Johir, M.B. Ahmed, Photocatalysis of estrone in water and wastewater: Comparison between Au-TiO_2 nanocomposite and TiO_2, and degradation by-products. Sci. Total Environ. 610-611 (2018) 521-530.
[10] A. Serrà, L. Philippe, F. Perreault, S. Garcia-Segura, Photocatalytic treatment of natural waters. Reality or hype? The case of cyanotoxins remediation. Water Res. 188 (2021) 116543.
[11] M. Gar Alalm, M. Samy, S. Ookawara, T. Ohno, Immobilization of S-TiO_2 on reusable aluminum plates by polysiloxane for photocatalytic degradation of 2,4-dichlorophenol in water. J. Water Process Eng. 26 (2018) 329-335.
[12] M. Samy, M.G. Ibrahim, M. Fujii, K.E. Diab, M. ElKady, M. Gar Alalm, CNTs/MOF-808 painted plates for extended treatment of pharmaceutical and agrochemical wastewaters in a novel photocatalytic reactor. Chem. Eng. J. 406 (2021) 127152.
[13] J. Lim, H. Kim, J. Park, G.-H. Moon, J.J.M. Vequizo, A. Yamakata, J. Lee, W. Choi, How g-C3N4 works and is different from TiO_2 as an Environmental Photocatalyst: Mechanistic View. Environ. Sci. Technol. 54 (2020) 497-506.
[14] S.K. Loeb, P.J.J. Alvarez, J.A. Brame, E.L. Cates, W. Choi, J. Crittenden, D.D. Dionysiou, Q. Li, G. Li-Puma, X. Quan, D.L. Sedlak, T. David Waite, P. Westerhoff, J.H. Kim, The technology horizon for photocatalytic water treatment: Sunrise or sunset?. Environ. Sci. Technol. 53 (2019) 2937-2947.
[15] A. Kumar, M. Khan, J. He, I.M.C. Lo, Recent developments and challenges in practical application of visible–light–driven TiO_2–based heterojunctions for PPCP degradation: A critical review. Water Res. 170 (2020) 115356.
[16] H. Khan, Z. Jiang, D. Berk, Molybdenum doped graphene/TiO_2 hybrid photocatalyst for UV/visible photocatalytic applications. Sol. Energy 162 (2018) 420-430.
[17] R. Lahiri, A. Ghosh, B. Choudhuri, A. Mondal, Investigation on improved performance of Erbium doped TiO_2 nanowire based UV detector. Mater. Res. Bull. 103 (2018) 259-267.
[18] M.M. Rashad, E.M. Elsayed, M.S. Al-Kotb, A.E. Shalan, The structural, optical, magnetic and photocatalytic properties of transition metal ions doped TiO_2 nanoparticles. J. Alloys and Compd. 581 (2013) 71-78.
[19] N.C. Birben, M.C. Paganini, P. Calza, M. Bekbolet, Photocatalytic degradation of humic acid using a novel photocatalyst: Ce-doped ZnO. Photochem. Photobiol. Sci. 16 (2017) 24-30.
[20] P. Mazierski, A. Mikolajczyk, B. Bajorowicz, A. Malankowska, A. Zaleska-Medynska, J. Nadolna, The role of lanthanides in TiO_2-based photocatalysis: A review. Appl. Catal. B: Environ. 233 (2018) 301-317.
[21] F.B. Li, X.Z. Li, M.F. Hou, K.W. Cheah, W.C.H. Choy, Enhanced photocatalytic activity of

Ce^{3+}–TiO_2 for 2-mercaptobenzothiazole degradation in aqueous suspension for odour control. Appl. Catal. A: Gen. 285 (2005) 181-189.
[22] J. Xie, D. Jiang, M. Chen, D. Li, J. Zhu, X. Lu, C. Yan, Preparation and characterization of monodisperse Ce-doped TiO_2 microspheres with visible light photocatalytic activity. Colloids and Surfaces A: Physicochem. Eng. Asp. 372 (2010) 107-114.
[23] P. Sun, L. Liu, S.C. Cui, J.G. Liu, Synthesis, characterization of Ce-doped TiO_2 nanotubes with high visible light photocatalytic activity. Catal. Lett. 144 (2014) 2107-2113.
[24] A. Jafari, S. Khademi, M. Farahmandjou, Nano-crystalline Ce-doped TiO_2 powders: sol-gel synthesis and optoelectronic properties. Mater. Res. Express 5 (2018) 095008.
[25] R.R. Nair, J. Arulraj, K.R.S. Devi, Ceria doped titania nano particles: Synthesis and photocatalytic activity. Mater. Today: Proc. 3 (2016) 1643-1649.
[26] G.B. Vieira, G. Scaratti, F.S. Rodembusch, S.M.D. Amorim, M. Peterson, G.L. Puma, R.D.F.P.M. Moreira, Tuning the photoactivity of TiO_2 nanoarchitectures doped with cerium or neodymium and application to colour removal from wastewaters. Environ. Technol. (2019) 1-15.
[27] F. Mikaeili, S. Topcu, G. Jodhani, P.I. Gouma, Flame-sprayed pure and Ce-doped TiO_2 photocatalysts. Catalysts 8 (2018) 1-12.
[28] N. Yan, Z. Zhu, J. Zhang, Z. Zhao, Q. Liu, Preparation and properties of ce-doped TiO_2 photocatalyst. Mater. Res. Bull. 47 (2012) 1869-1873.
[29] M.J. Munoz-Batista, M.d.l.M. Ballari, A. Kubacka, A.E. Cassano, O.M. Alfano, M. Fernandez-Garcia, Acetaldehyde degradation under UV and visible irradiation using CeO_2–TiO_2 composite systems: Evaluation of the photocatalytic efficiencies. Chem. Eng. J. 255 (2014) 297-306.
[30] M. Sidheswaran, L.L. Tavlarides, Characterization and visible light photocatalytic activity of cerium- and iron-doped titanium dioxide sol−gel materials. Ind. Eng. Chem. Res. 48 (2009) 10292-10306.
[31] H. Khan, N. Usen, D.C. Boffito, Spray-dried microporous Pt/TiO_2 degrades 4-chlorophenol under UV and visible light. J. Environ. Chem. Eng. 7 (2019) 103267.
[32] H. Khan, M.G. Rigamonti, G.S. Patience, D.C. Boffito, Spray dried TiO_2/WO_3 heterostructure for photocatalytic applications with residual activity in the dark. Appl. Catal. B: Environ. 226 (2018) 311-323.
[33] N. Saadatkhah, M.G. Rigamonti, D.C. Boffito, H. Li, G.S. Patience, Spray dried SiO_2 WO_3/TiO_2 and SiO_2 vanadium pyrophosphate core-shell catalysts. Powder Technol. 316 (2017) 434-440.
[34] D. Meroni, C. Gasparini, A.D. Michele, S. Ardizzone, C.L. Bianchi, Ultrasound-assisted synthesis of ZnO photocatalysts for gas phase pollutant remediation: Role of the synthetic parameters and of promotion with WO_3. Ultraso. Sonochem. 66 (2020) 105119.
[35] M. Stucchi, D.C. Boffito, E. Pargoletti, G. Cerrato, C.L. Bianchi, G. Cappelletti, Nano-MnO_2 decoration of TiO_2 microparticles to promote gaseous ethanol visible photoremoval. Nanomaterials 8 (2018) 686.
[36] G. Xiao, J. Zhou, X. Huang, X. Liao, B. Shi, Facile synthesis of mesoporous sulfated Ce/TiO_2 nanofiber solid superacid with nanocrystalline frameworks by using collagen fibers as a biotemplate and its application in esterification. RSC Adv. 4 (2014) 4010-4019.
[37] M.B. Marami, M. Farahmandjou, Water-based sol–gel synthesis of Ce-doped TiO_2 nanoparticles. J. Electron. Mat. 48 (2019) 4740-4747.
[38] H.G. Yang, C.H. Sun, S.Z. Qiao, J. Zou, G. Liu, S.C. Smith, H.M. Cheng, G.Q. Lu, Anatase TiO_2 single crystals with a large percentage of reactive facets. Nature 453 (2008) 638-641.

[39] H. Khan, M.G. Rigamonti, D.C. Boffito, Enhanced photocatalytic activity of Pt-TiO_2/WO_3 hybrid material with energy storage ability. Appl. Catal. B: Environ. 252 (2019) 77-85.
[40] L.H. Little, H.W. Salzberg, Infrared spectra of absorbed species, J. Electrochem. Soc. 114 (1967) 279C.
[41] C. Morterra, An infrared spectroscopic study of anatase properties. Part 6. Surface hydration and strong Lewis acidity of pure and sulphate-doped preparations. J. Chem. Soc. Faraday Trans. 1: Phys. Chem. Cond. Phases 84 (1988) 1617-1637.
[42] C. Morterra, V. Bolis, E. Fisicaro, The hydrated layer and the adsorption of CO at the surface of TiO_2 (anatase). Colloids Surf. 41 (1989) 177-188.
[43] J. Dhanalakshmi, S. Iyyapushpam, S.T. Nishanthi, M. Malligavathy, P.D. Pathinettam, Investigation of oxygen vacancies in Ce coupled TiO_2 nanocomposites by Raman and PL spectra. Adv. Nat. Sci-Nanosci. Nanotech. 8 (2017) 015015.
[44] S.W. Chen, J.M. Lee, K.T. Lu, C.W. Pao, J.F. Lee, T.S. Chan, J.M. Chen, Band-gap narrowing of TiO_2 doped with Ce probed with x-ray absorption spectroscopy. Appl. Phys. Lett. 97 (2010) 012104.
[45] S. Umrao, S. Abraham, F. Theil, S. Pandey, V. Ciobota, P.K. Shukla, C.J. Rupp, S. Chakraborty, R. Ahuja, J. Popp, B. Dietzek, A. Srivastava, A possible mechanism for the emergence of an additional band gap due to a Ti–O–C bond in the TiO_2–graphene hybrid system for enhanced photodegradation of methylene blue under visible light. RSC Adv. 4 (2014) 59890-59901.
[46] G. Greczynski, L. Hultman, C 1s peak of adventitious carbon aligns to the vacuum level: dire consequences for material's bonding assignment by photoelectron spectroscopy. ChemPhysChem 18 (2017) 1507-1512.
[47] R. Ren, Z. Wen, S. Cui, Y. Hou, X. Guo, J. Chen, Controllable synthesis and tunable photocatalytic properties of Ti^{3+}-doped TiO_2. Sci. Rep. 5 (2015) 10714.
[48] H. Tan, Z. Zhao, M. Niu, C. Mao, D. Cao, D. Cheng, P. Feng, Z. Sun, A facile and versatile method for preparation of colored TiO_2 with enhanced solar-driven photocatalytic activity. Nanoscale 6 (2014) 10216-10223.
[49] G.B. Vieira, H.J. Jose, M. Peterson, V.Z. Baldissarelli, P. Alvarez, P.M.M.R. de Fatima, CeO_2/TiO_2 nanostructures enhance adsorption and photocatalytic degradation of organic compounds in aqueous suspension. J. Photochem. Photobiol. A: Chem. 353 (2018) 325-336.
[50] Z. Liu, B. Guo, L. Hong, H. Jiang, Preparation and characterization of cerium oxide doped TiO_2 nanoparticles. J. Phys. Chem. Sol. 66 (2005) 161-167.
[51] Y. Nosaka, M. Nishikawa, A.Y. Nosaka, Spectroscopic investigation of the mechanism of photocatalysis. Molecules 19 (2014) 18248-18267.
[52] C. Fan, P. Xue, Y. Sun, Preparation of nano-TiO_2 doped with cerium and its photocatalytic activity. J. Rare Earths 24 (2006) 309-313.
[53] Y. Zhang, A.H. Yuwono, J. Wang, J. Li, Enhanced photocatalysis by doping cerium into mesoporous titania thin films. J. Phys. Chem. C 113 (2009) 21406-21412.
[54] G. Fu, P. Zhou, M. Zhao, W. Zhu, S. Yan, T. Yu, Z. Zou, Carbon coating stabilized Ti^{3+}-doped TiO_2 for photocatalytic hydrogen generation under visible light irradiation. Dalt. Trans. 44 (2015) 12812-12817.
[55] H. Khan, I.M. Swati, Fe^{3+}-doped anatase TiO_2 with d–d transition, oxygen vacancies and Ti^{3+} centers: Synthesis, characterization, UV–vis photocatalytic and mechanistic studies. Ind. Eng. Chem. Res. 55 (2016) 6619-6633.
[56] L.B. Xiong, J.L. Li, B. Yang, Y. Yu, Ti^{3+} in the surface of titanium dioxide: generation,

properties and photocatalytic application. J. Nanomaterials 2012 (2012).
[57] N. Rozman, D.M. Tobaldi, U. Cvelbar, H. Puliyalil, J.A. Labrincha, A. Legat, A.S. Skapin, Hydrothermal synthesis of rare-earth modified titania: Influence on phase composition, optical properties, and photocatalytic activity. Materials 12 (2019) 713.